# Accepted Manuscript

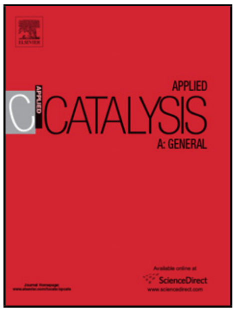

Title: Product tunable behavior of carbon nanotubes-supported
Ni−Fe catalysts for guaiacol hydrodeoxygenation

Author: Huihuang Fang Jianwei Zheng Xiaolin Luo Junmou
Du Alberto Roldan Stefano Leoni Youzhu Yuan

PII: S0926-860X(16)30503-8
DOI: http://dx.doi.org/doi:10.1016/j.apcata.2016.10.011
Reference: APCATA 16027

To appear in: *Applied Catalysis A: General*

Received date: 16-6-2016
Revised date: 6-10-2016
Accepted date: 12-10-2016

Please cite this article as: Huihuang Fang, Jianwei Zheng, Xiaolin Luo, Junmou Du, Alberto Roldan, Stefano Leoni, Youzhu Yuan, Product tunable behavior of carbon nanotubes-supported Ni−Fe catalysts for guaiacol hydrodeoxygenation, Applied Catalysis A, General http://dx.doi.org/10.1016/j.apcata.2016.10.011

# Product tunable behavior of carbon nanotubes-supported Ni–Fe catalysts for guaiacol hydrodeoxygenation

Huihuang Fang[1], Jianwei Zheng[1], Xiaolin Luo[1] Junmou Du[1], Alberto Roldan[2], Stefano Leoni[2]*, Youzhu Yuan[1]*

[1] *State Key Laboratory of Physical Chemistry of Solid Surfaces, National Engineering Laboratory for Green Chemical Productions of Alcohols-Ethers-Esters and iChEM, College of Chemistry and Chemical Engineering, Xiamen University, Xiamen, 361005, China*

[2] *School of Chemistry, Cardiff University, Main Building, Park Place, Cardiff, CF10 3AT, United Kingdom*

---

* To whom correspondence should be addressed. E-mail: yzyuan@xmu.edu.cn, LeoniS@cardiff.ac.uk

## Graphical abstract

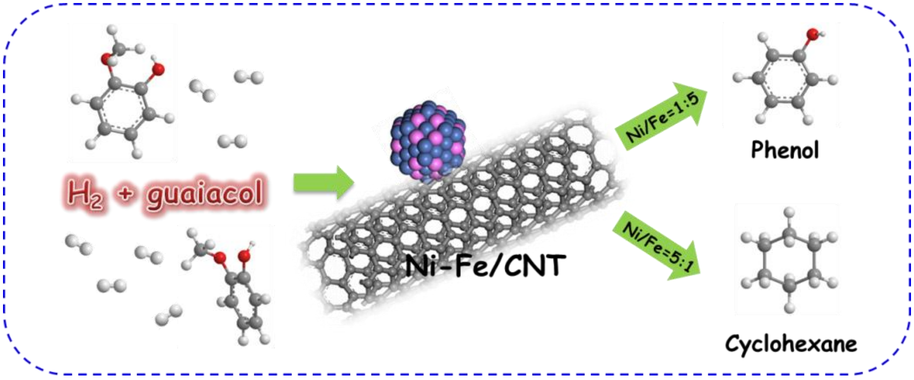

## Highlights:

- Non-noble Ni-Fe bimetallic catalysts are preparation by varying Ni/Fe ratios.
- Ni-Fe/CNT shows higher performance for guaiacol HDO than mono-metal catalysts.
- High selectivity to cyclohexane or phenol is tunable by varying the Ni/Fe ratios.
- The enhanced performance is ascribed to the synergism Ni and Fe in Ni-Fe alloy.

## Abstract

Bimetallic Ni–Fe nanoparticles supported on carbon nanotubes (CNTs) are prepared and evaluated for the catalytic hydrodeoxygenation (HDO) of a lignin-derived model compound guaiacol. Appropriate combination of Ni and Fe affords high activity and significantly enhances selectivity to cyclohexane or phenol, whereas monometallic Ni and Fe catalysts display poor activities or selectivities. The product tunable behavior of guaiacol HDO is found to be dependent on Ni/Fe atomic ratios. Cyclohexane and phenol are the major products over $Ni_5$–$Fe_1$/CNT with Ni/Fe atomic ratio at 5/1 and $Ni_1$–$Fe_5$/CNT with Ni/Fe atomic ratio at 1/5, respectively. Characterization results confirm that Ni–Fe alloys are formed and elicit synergistic effects on the HDO performance. The selectivity-switchable performance of Ni–Fe/CNT can be assigned to the synergism between Ni domains, where $H_2$ can be easily activated, and Fe domains, which exhibited strong oxophilicity. The bimetallic catalysts give an enhanced stability without significant sintering of metal nanoparticles, while the monometallic catalysts show obvious deactivation due to the agglomeration of metal nanoparticles. Further results reveal that the conversion of guaiacol depends on not only the chemical state but also the size of the metallic nanoparticles. The catalysts with appropriate Ni/Fe atomic ratio and smaller particle perform better hydrogenolysis of C–O bonds, resulting in high selectivity to cyclohexane or phenol.

**Keywords:** Ni–Fe catalyst; hydrodeoxygenation; guaiacol; cyclohexane; phenol

## 1. Introduction

Renewable feedstocks, such as lignocellulose, have gained considerable attention for sustainable production of fuel and chemicals because of the limited availability and passive effect of fossil fuels [1–5]. Lignin, an amorphous tri-dimensional biopolymer containing abundant methoxylated propyl phenol units, is the second most important compound in lignocellulosic biomass (15%–20%) [6]. In contrast to cellulose and hemicellulose, lignin is the most similar to petroleum in structure and composition, which is industrially available from biomass-to-ethanol processes and other biorefineries [7]. Generally, lignocellulosic biomass is directly converted into aromatics and bio-oils through a traditional method known as rapid pyrolysis [3]. However, the methoxylated propyl phenol unit contains numerous $C_{aryl}$–$OCH_3$, $C_{aryl}$–OH, and $C_{aryl}$–OR bonds; as such, the pyrolysis product is comprised high amounts of oxygen and oxo-functionalized groups than commercial fuel and thus presents limited applications [8]. In addition, lignin-derived phenolic compounds are highly reactive during fast pyrolysis, which leads to the formation of oligomers and deactivation of catalysts [9,10]. Therefore, upgrading of bio-oils through hydrodeoxygenation (HDO) with hydrogen consumption is valuable [11].

Guaiacol, a model compound of lignin-derived bio-oils, contains two types of O-containing functional groups ($C_{aryl}$–$OCH_3$ and $C_{aryl}$–OH), which are characteristic components of lignin-derived compounds [12,13]. Hence, the catalytic hydrogenolysis and HDO of guaiacol have gained increased research attention to elucidate the roles of catalysts and identify their industrial applications.

Metal sulfides, such as $MoS_2$, NiMoS, and CoMoS, as well as supported noble metals, such as Ru, Pt, and Pd which are widely used in hydrodesulfurization, are also applied in HDO because of their similarity to S and O [14,15]. Metal sulfides exhibit satisfactory activities but deactivate rapidly, especially during the formation of water as the byproduct [2,6,16]. The activated sulfide form of catalysts is maintained through continuous addition of S to the reactant stream, causing serious negative effects on downstream processes [17,18]. Using noble metals for HDO of guaiacol could avoid these problems [11,13,19,20]. Gates et al. [21,22] used Pt catalysts for HDO of lignin-derived species and reported that hydrogenolysis of C–O bonds is the most kinetically available route that does not remove oxygen. Varma et al. [23] systematically surveyed the HDO of guaiacol on noble metal catalysts; the developed Pt/C catalysts showed superior activity at the optimal operating temperature of 573 K. Supported noble metal catalysts demonstrate satisfactory activity but have limited applications because of the high cost of noble metals. Hence, novel metal catalysts such as non-noble metallic catalysts should be developed for economic viability and engineering aspects.

Ni is cheaper than noble metals and shows high activity in hydrogenation reactions; as such, this element is widely used as a metallic catalyst [24–28]. Zhao et al. [27] reported that Ni/HZSM exerts synergistic effects on HDO and C–O bond cleavage of substituted phenols. Ma et al. [24] investigated Ni-based catalysts supported by mixed oxides and found that Ni/$TiO_2$–$ZrO_2$ displayed the optimal performance, with a cyclohexane yield of 86.4% in the solvent decalin at 573 K and 4.0 MPa $H_2$. Recently, Dongil et al. [29] obtained tunable selectivities of cyclohexane and cyclohexene over CNTs supported Ni nanoparticles inside and outside. On the other hand, several reports also indicated that Fe was active in selective cleavage of aryl C–O bonds [25,26]. Olcese et al. [26] found that the Fe/$SiO_2$ catalyst was efficient for the guaiacol HDO. However, these mono-metallic catalysts exhibit inherent low activity and poor stability. In this regard, a second metal is added to form bimetallic nanoparticles, such as Ni–Cu, Pt–Sn and Pd–Fe, which can remarkably promote catalytic properties as a result of geometric and electronic effects [28,30]. Ardiyanti et al. [28] found that bimetallic catalysts promoted higher HDO activity than the mono-metallic Ni and Cu catalysts for hydrotreatment of anisole over Ni–Cu catalysts; Sun et al. [30] reported that Pd–Fe/C bimetallic catalyst benefit the HDO of guaiacol to benzene with 83.2% yield at 723 K.

In this study, bimetallic Ni–Fe catalysts supported on carbon nanotubes (CNTs) were prepared and firstly applied to investigate the relationship between the bimetallic structure and the HDO performance of guaiacol, particularly selectivity. In all cases, CNTs are used as carriers due to their special electrical properties, hydrogen spillover, and chemical stability, which have triggered wide research interest [31,32]. Product distribution was correlated with the amounts of Ni and Fe. The synthesized catalysts displayed tunable selectivity to cyclohexane or phenol at Ni/Fe atomic ratio of 5/1 or 1/5, respectively. Further experiments including powder X-ray diffraction (XRD), $H_2$-temperature-programmed reduction ($H_2$-TPR), transmission electron microscopy (TEM), X-ray photoelectron spectroscopy (XPS), high-sensitivity low-energy ion scattering spectroscopy (HS-LEIS), Raman spectroscopy, and computational modelling were performed to elucidate the interaction between Ni and Fe. The results revealed the key role of different metals on the HDO pathway and confirmed the synergistic effect of Ni–Fe alloy nanoparticles, in which the Ni domains demonstrated high ability to activate $H_2$ and the Fe domain displayed strong oxophilicity. Meanwhile, deactivation of monometallic catalysts was observed which may be ascribed to the agglomeration of nanoparticles. Size effects of the catalysts were further investigated.

## 2. Experimental

### 2.1. Catalyst preparation

CNTs with 97% purity were purchased from Shenzhen Nanotech Port Co., Ltd. The obtained CNTs have parallel multiwall structures with an outer diameter of 20–40 nm. Prior to use, the as-received CNTs were pretreated in concentrated $HNO_3$ (68 wt. %) at 353 K for 16 h under reflux conditions to remove residual catalysts and amorphous carbons. The treated CNTs were thoroughly washed with a large quantity of deionized water until the pH became neutral and then dried overnight. All other carbon materials before use were pretreated in the same process as above.

Ni–Fe bimetallic catalysts were prepared through co-impregnation using aqueous solutions of $Ni(NO_3)_2 \cdot 6H_2O$ and $Fe(NO_3)_3 \cdot 9H_2O$. The total loading weight of metal was maintained at 7 wt. %, and the Ni/Fe atomic ratio was accordingly adjusted. Typically, 1.0 g of CNTs was added to 30 mL of distilled water containing required amounts of $Ni(NO_3)_2 \cdot 6H_2O$ and $Fe(NO_3)_3 \cdot 9H_2O$ with vigorous stirring for 6 h. Then, the aqueous solution removed the excess solvent by evaporation to keep an incipient wetness liquid/solid ratio of 1 mL $g^{-1}$. After impregnation for 12 h at room temperature and solvent removal by evaporation, the mixture was dried at 373 K overnight. All dry solids were calcined for 4 h at 573 K with a heating ramp of 2 K $min^{-1}$ in the atmosphere. The catalysts were reduced by 5% $H_2$–95% $N_2$ (25 mL $min^{-1}$) for 4 h prior to the reaction. The bimetallic catalyst was denoted as $Ni_x$–$Fe_y$/CNT, where x and y represent the atomic ratios of Ni and Fe, respectively. Monometallic catalysts, namely, Ni/CNT and Fe/CNT, were prepared using the same method.

### 2.2. *Catalyst characterization*

Ni and Fe contents of the catalysts were determined through inductively coupled plasma optical emission spectrometry (ICP-OES) using a Thermo Elemental IRIS Intrepid II XSP. The samples were pretreated with aqua regia at 353 K for 1 h, and the remaining solution was heated to remove the solvent. The residues were diluted with 5% $HNO_3$ and filtered in a 50 mL volumetric flask before measurement.

Specific surface area, pore volume and average pore diameter were measured by static $N_2$ physisorption method at 77.3 K on a Micromeritics TriStar II 3020 surface area and pore analyzer. The sample was degassed at 573 K for 3 h prior to the measurements. Specific surface area was determined through Brunauer-Emmett-Teller (BET) method. Pore size and average pore diameter distributions were calculated from the desorption isotherm branch according to the Barret-Joyner-Halenda (BJH) method. The total pore volume of the samples depended on the adsorbed $N_2$ volume at a relative pressure of approximately 0.99.

Powder XRD patterns were obtained on a Phillips PANalytical X'pert Pro diffractometer equipped with a graphite monochromator and Cu−$K_\alpha$ radiation (40 kV and 30 mA) at scanning 2θ from 10° to 90°. The obtained diffraction data were identified and compared with reference patterns in the JCPDS database.

$H_2$-TPR spectra were determined using a Micromeritics AutoChem II 2920 chemisorption analyzer. The sample was pretreated in Ar (30 mL $min^{-1}$) at 573 K for 30 min and then cooled to room temperature. The reducing gas (5% $H_2$−95% $N_2$) was then flowed through the sample at a rate of 30 mL/min, and the ambient temperature was raised to 1173 K at a rate of 10 K $min^{-1}$. A thermal conductivity detector was used to monitor $H_2$

consumption.

TEM studies were performed using an electron microscope (Philips Analytical FEI Tecnai 20) operated at an acceleration voltage of 300 kV. The samples for TEM analysis were ultrasonically dispersed in ethanol. Drops of the suspension were deposited on copper grids coated with C films.

XPS spectra were recorded on an Omicron Sphera II photoelectron spectrometer equipped with an Al–$K_\alpha$ X-ray radiation source (hν = 1486.6 eV). The machine is connected to HS-LEIS, in which measurement was performed by IONTOF Qtac100 using $20Ne^+$ (5 keV) as Fe source. The scattering angle was 145°. The sample was treated in an *in situ* chamber with 5% $H_2$–95% $N_2$ at 673 K for 4 h before the measurement. All measurements were performed in a system with combined elevated pressure reaction cell and ultrahigh vacuum (UHV). Sample preparation and characterization were conducted in the primary UHV chamber (base pressure, $7 \times 10^{-9}$ Torr).

Raman spectra were obtained using a Renishaw inVia Raman microscope equipped with an Ar ion laser at an excitation wavelength of 514 nm and a laser source intensity of 10%.

### *2.3. Catalytic testing*

The catalytic reactions for HDO were performed on a conventional fixed-bed flow reactor equipped with an auto-sampling system (Figure S1). Briefly, 100 mg of the as-calcined catalyst was placed in the center of the reaction tube and sandwiched by quartz powders. Prior to the experiment, the catalyst precursor was reduced under 5% $H_2$–95%

$N_2$ at 673 K for 240 min at a ramping rate of 3 K $\text{min}^{-1}$. After cooling the catalyst bed to the reaction temperature, pure $H_2$ was fed into the reactor and held at 3.0 MPa. For the HDO reaction, pure guaiacol was pumped into the reactor with varying weight liquid hourly space velocity ($\text{WLHSV}_{\text{GUA}}$) by using a Series III digital HPLC pump (Scientific Systems, Inc.). Then, the introduced guaiacol reacted with $H_2$ at the catalyst bed. The product line was heated at 583 K before cold trap to avoid condensation of liquid products. An Agilent 7890A gas chromatograph (GC), equipped with an auto-sampling valve, DB-Wax (30 m × 0.32 mm × 0.25 μm) capillary column, and flame ionization detector (FID) was used to analyze the products. The mixture collected through condensation was analyzed by an Agilent 7890GC-5975MS system. After the condensation of the products, the dry gas was conveyed into a GC 2060 with a TDX column and thermal conductivity detector for analysis of gas products (CO, $CH_4$, $CO_2$, and $H_2O$). The response factors of guaiacol and products were determined using pure compounds with known concentrations. The carbon balance was about 95% ± 2%, unless otherwise noted. Guaiacol conversion ($X_{\text{GUA}}$), selectivity to C6 ring products ($S_{\text{C6i}}$) and selectivity to C1 products ($S_{\text{C1i}}$) were calculated as follows:

$$X_{\text{GUA}} = \frac{(\text{moles of GUA})_{\text{in}} - (\text{moles of GUA})_{\text{out}}}{(\text{moles of GUA})_{\text{in}}} \times 100\% \qquad \text{Eq. 1}$$

$$S_{\text{C6i}} = \frac{\text{moles of ring product i}}{\text{the sum moles of guaiacol consumed}} \times 100\% \qquad \text{Eq. 2}$$

$$S_{\text{C1i}} = \frac{\text{moles of produced methane or methanol}}{\text{the sum moles of guaiacol consumed}} \times 100\% \qquad \text{Eq. 3}$$

Unless otherwise mentioned, the reported conversion and selectivity were obtained after the reaction proceeded for 2 h when the ready state was reached. $S_{C6i}$ was calculated based on the number of C6 rings except for C1 products ($CH_4$ and $CH_3OH$); $S_{C1i}$ was calculated based on the number of methoxy groups from the reacted substrate. In some cases, the total selectivity to C1 products is less than 100% because of the formation of coke or trace transalkylation reaction. The turnover frequency (TOF) was based on the metal dispersion, indicating the moles of guaiacol converted by per atom at the catalyst surface per hour (mol-guaiacol mol-metal$_{surf}^{-1}$ h$^{-1}$, for short, h$^{-1}$). The guaiacol conversion for the TOF calculation was lower than 40%.

### *2.4. Computational modelling*

The catalyst surface was simulated with a periodic slab model of Ni exposing the most stable surface (111). Each slab represents a *p(3x3)* cell with an area of 44.6478 Å$^2$ and five atomic layers where the top two are fully relaxed while the bottom surface remain fix at the optimized interatomic distance simulating the bulk. A vacuum of 15 Å avoids the interactions between the slab and its images. As a doped model, we replaced three Ni from the pristine surface with Fe. We studied two different configurations and found that an alternating distribution of Fe atoms is 0.19 eV more stable than Fe agglomeration. To obtain the properties of isolated molecules, we placed them in the center of a 19x20x21 Å$^3$ simulation cell to avoid lateral interactions, with broken symmetry, and using the same criteria of convergence as for the metallic surfaces.

All calculations were carried out with the density-functional theory-D2 (DFT-D2) as implemented in the Vienna ab initio simulation package (VASP) [33,34]. The Kohn-Sham valence states were expanded in a plane-wave basis set with a cut off at 450 eV for the kinetic energy [35]. The electron exchange-correlation was denoted by the generalized gradient approximation (GGA) with the Perdew-Burke-Ernzerhof revised for solids (PBEsol) [36]. All the calculations include long-range dispersion correction Grimme approach [37], which is an improvement on standard DFT [38–40]. A Monkhorst-Pack grid of 5x5x1 k-points was used to evaluate the wavefunctions which ensures the electronic and ionic convergence [41]. The systems were considered converged when the force on each ion dropped below 0.01 eV/Å and the energy threshold defining self-consistency of the electron density was set to $10^{-5}$ eV.

We have calculated the energy variations (ΔE) along the reaction pathway according to Eq. 4, $E_{System}$ being the energy of the slab and adsorbates, $E_{Surf}$ the energy of the naked slab, $E_{Gua}$ and $n.E_{H2}$ the energy of the isolated guaiacol and $H_2$ molecules.

$$E_B = E_{System} - \left(E_{Surf} + E_{Gua} + n \cdot E_{H_2}\right) \qquad \text{Eq. 4}$$

## 3. Results and discussion

### *3.1. Catalyst characterization*

A series of supported Ni–Fe bimetallic catalysts were prepared with a fixed total metal loading (7 wt. %) but varied Ni/Fe atomic ratios. The physicochemical properties of the catalysts are summarized in Table 1. The ICP-OES results show that actual metal loading is similar to the preset values in the preparation. The BET surface area of CNTs is approximately 147 $m^2$ $g^{-1}$, and all surface areas of catalysts approximate those of CNTs after loading with metals.

The XRD patterns of the samples after reduced under 5% $H_2$–95% $N_2$ at 673 K for 4 h are shown in Figures 1 and S2. Distinct diffraction peaks of the metal Ni species are observed at $2\theta = 44.50°$, 51.60°, 76.08°, which correspond to the (111), (200), and (220) reflections of the Ni phase (PDF 00-001-1258). No significant diffraction peaks of $Fe^0$ species are observed, probably due to their highly dispersion on the catalyst surfaces. The diffraction lines of the Ni–Fe alloy are similar to those of monometallic Ni and Fe, which exhibit similar face-centered cubic structures and lattice constants. The peak position corresponding to (111) are shifted to lower angles (from 44.50° to 43.90°) with increasing Fe content, indicating the formation of Ni–Fe alloy. This finding is consistent with the results previously reported [42,43]. In addition, diffraction peaks emerge at $2\theta = 44.28°$, 51.53°, 75.87° for bimetallic catalysts, which is ascribed to the diffractions of $Fe_1$–$Ni_3$ alloy phase (PDF 00-038-0419). With increasing Fe content, the diffraction peaks belonging to $Fe_3O_4$ ($2\theta = 30.06°$, 35.45°; PDF 00-001-1111) appear because of incomplete reduction of iron oxide at 673 K. The XRD patterns of samples after reduced at 773 K and 873 K are shown in Figures S3 and S4, respectively. The diffraction peak at $2\theta = 44.64°$ belonging to $Fe^0$ species appears while the $Fe_3O_4$ phase disappears when all the samples were reduced at 873 K, indicating that iron oxides can be completely reduced at this temperature.

The average diameters of nanoparticles reduced at 673 K, 773 K, and 873 K based on the Scherrer equation are summarized in Tables 1 and 2. Crystallite size decreases with increase amount of Fe, suggesting that Fe promoted the dispersion of metallic Ni. Further, the nanoparticle size increases with the increase of reduction temperatures. Figure S5-a–f shows the TEM images and metallic particle size distribution of 673 K-reduced catalysts containing varied Ni/Fe atomic ratios. The mean particle sizes of monometallic Ni/CNT and Fe/CNT are 8.7 and 5.1 nm, respectively. The average particle sizes of bimetallic particles are smaller than that of Ni/CNT and decreased (7.3, 6.9, 6.2, and 5.3 nm at a Ni/Fe ratio of 5/1, 2/1, 1/1, and 1/5, respectively) with decreasing Ni/Fe atomic ratio. Both the XRD and TEM results indicate that Fe species is beneficial for Ni dispersion.

The microstructure of $Ni_5$–$Fe_1$/CNT was characterized using high-resolution TEM (HRTEM) and scanning transmission electron microscope-energy dispersive X-ray (STEM-EDX) elemental mapping and linear scanning pattern to observe distribution of Ni and Fe in bimetallic catalysts (Figure 2). The representative HRTEM image (Figure 2-a) shows a 0.205 nm distance between the corresponding lattice fringes, and this distance is consistent with the lattice spacing of Ni–Fe alloy [42]. The results of nanoscale elemental STEM-EDX mapping and linear scanning analyses are shown in Figure 2-b–c. Ni is well distributed throughout the Fe domain, indicating that Ni and Fe are homogeneous distributed along the bimetallic particles. Ni species display improved distribution than Fe possibly because some $Fe_3O_4$ particles were not reduced completely. The linear scanning analysis also confirms the mapping results. The distribution of Ni is similar to that of Fe in an individual particle, and the formation of Ni–Fe alloy in the Fe domain was verified. The HRTEM image and STEM-EDX line scanning analysis of $Ni_1$–$Fe_5$/CNT catalyst are also verified the formation of Ni–Fe alloys (Figure S6). These results are consistent with the XRD patterns and the computational models.

In situ XPS and HS-LEIS analyses were performed to determine the structure and electronic properties of Ni–Fe nanoparticles. The Ni 2p and Fe 2p spectra of Fe/CNT, Ni/CNT, $Ni_2$–$Fe_1$/CNT, and $Ni_5$–$Fe_1$/CNT are displayed in Figure 3. Data on XPS curve fitting are summarized in Table S1. All XPS peaks are identified according to published data and an on-line database (www.lasurface.com). In contrast to those of bimetallic Ni–Fe/CNT samples, the Fe 2p spectra of Fe/CNT [Figure 3(A)-a] show a binding energy of Fe $2p_{3/2}$ at 711.0 eV and that of Fe $2p_{1/2}$ at 724.0 eV, a typical characteristic of $Fe^{3+}$. To check the rationality of peak-fitting we executed the curve-fitting by fitting two peaks at 707.3 and 709.0 eV. The results became worse, indicating that only $Fe^{3+}$ exists on the surface of Fe/CNT sample. Hence, Fe species supported on CNTs are hardly reduced at 673 K within 4 h. Nevertheless, the results for bimetallic Ni–Fe/CNT samples reveal that the Fe 2p spectra evidently change [Figure 3(A)-b–c]. Three peaks of the binding energy of Fe $2p_{3/2}$ are identified at 707.3, 709.0, and 711.0 eV for $Ni_2$–$Fe_1$/CNT and $Ni_5$–$Fe_1$/CNT. In addition, a binding energy of approximately 715.0 eV is ascribed to the satellite peak of $Fe^{2+}$ species, and is commonly observed in $Fe^{2+}$ compounds. The original peaks at 707.3 and 709.0 eV are ascribed to the binding energy of $Fe^0$ and $Fe^{2+}$, respectively; this finding indicates that some $Fe^{3+}$ species are reduced into FeO and $Fe^0$ in the presence of Ni species. Thus, Ni addition promotes the reduction of iron oxides. On the other hand, the binding energy of Ni 2p are observed at 853.1, 854.7, and 856.7 eV for monometallic Ni/CNT [Figure 3(B)-a]; these peaks are attributed to $Ni^0$, $Ni^{2+}$, and $Ni^{3+}$, respectively. The results indicate that a certain proportion of nickel oxides still exist when the sample was reduction at 673 K [44,45]. Figure 3(B)-b–c shows the XPS results of $Ni_2$–$Fe_1$/CNT, and

$Ni_5$–$Fe_1$/CNT. In these cases, the significant intensity due to the contribution of $Ni^0$ suggests that Ni oxides are more easily reduced than Fe ones under identical reduction condition.

Ni and Fe concentrations were calculated by peak fitting (Table S1). Bimetallic Ni–Fe/CNT catalysts display higher concentrations of $Fe^0$ and $Ni^0$ than those in the monometallic Fe/CNT or Ni/CNT catalysts. Values increase with increasing Fe content. The higher metallic Ni concentration in bimetallic Ni–Fe/CNT samples demonstrates the improved reducibility than that of monometallic Ni/CNT. The introduction of Fe does not inhibit but promote Ni reduction. As shown in Table 1, the Ni/Fe atomic ratios revealed by the XPS results are lower than those in the ICP-OES results, demonstrating that Fe easily segregates on the particle surface. Similarly, previous study [42] indicated that the cohesive energy of Ni is slightly higher than that of Fe. In addition, the HS-LEIS results show that Ni coexists with Fe on the outermost surface of Ni–Fe nanoparticles even if Fe will segregate on the surface (Figure S7). Therefore, it is presumable that the $Fe^0$ species interact with $Ni^0$ by forming Ni–Fe alloys and are located on the Ni domain, whereas the iron oxides are doped on the Ni–Fe nanoparticles. Table S2 shows the Ni/C and Fe/C atomic surface ratios of Ni–Fe/CNT catalysts from XPS peak fitting. The surface Ni/C atomic ratio represents the relative Ni dispersion on the surface of CNTs. Despite the lower loading of Ni, the surface Ni/C atomic ratio in $Ni_5$–$Fe_1$/CNT is higher than that of monometallic Ni/CNT catalyst (0.040 versus 0.021), which suggested that the introduction of Fe increases the Ni dispersion on the surface of support. These findings are consistent with the XRD and TEM results. Similar results were also observed in previous reports

[46,47].

Figure 4 shows the $H_2$-TPR reduction profiles of the as-calcined catalyst precursors containing different Ni/Fe ratios under a total metal loading of 7 wt. %. The monometallic Ni/CNT exhibits a distinct reduction peak at approximately 579 K with a shoulder peak at approximately 679 K. In previous reports [44,48,49], the reducibility of Ni species may be affected by the nature of the support used and the synthesis conditions. Zhang [48] et al. investigated the reduction of NiO deposited on CNTs and bulk NiO, suggesting that the reduction temperature of highly dispersed NiO nanoparticles is lower than bulk NiO. The first reduction peak of Ni/CNT at approximately 579 K is assigned to the reduction of highly dispersed NiO nanoparticles, and the shoulder peak is assignable to the reduction of larger NiO particles or some bulk-like NiO. The $H_2$-TPR reduction profile of Fe/CNT is different from those of the other samples. We observed that a tiny reduction peak appeared at approximately 667 K over Fe/CNT catalyst, which is ascribed to the reduction of $Fe_2O_3$ to $Fe_3O_4$. However, the $H_2$ consumption is smaller than other catalysts, which means only trace $Fe^{3+}$ oxides were reduced. In addition, the reduction peak above 835 K is assigned to the reduction of iron oxides to $Fe^0$ species and the interaction of FeO with C species [42]. This result reveals that Fe species are more difficult to be reduced than the Ni species. The $H_2$ consumption peaks of the as-calcined samples containing different Ni/Fe ratios shift to low temperatures with increasing Ni content. Compared with Fe/CNT, $Ni_1$–$Fe_5$/CNT shows a larger $H_2$ consumption peak, demonstrating that Ni promotes the reduction of Fe species. Furthermore, with decreasing Ni/Fe atomic ratios, the shoulder peak of Ni disappears and forms a larger reduction peak, suggesting that the introduction of Fe can improve the Ni dispersion. It has been reported that close interaction between metal species can promote or inhibit the reduction of metal oxides [47,50]. In our case, Ni and Fe species possibly form Ni–Fe alloys and Ni efficiently dissociates $H_2$. In addition, $H_2$ consumption peak at 769 K decreases with decreasing Ni content; this finding is consistent with the $H_2$ consumption of amorphous C species and reduction in the C functional group in the presence of metals [46,51].

The defect densities of the synthesized Ni–Fe/CNT catalysts were verified through analysis of the Raman spectra (Figure S8). Two peaks with a shoulder peak are observed at approximately 1340 and 1571 $cm^{-1}$, which are ascribed to the disordered graphite structure (D-band) and the ideal graphitic lattice vibration mode of Raman-active $E_{2g}$ phonon of $sp^2$–C atoms (G-band), respectively. High $I_D/I_G$ ratios, denoted as R, suggest the high extent of defects in CNTs. The $I_D/I_G$ ratios for original and pretreated CNTs are 0.77 and 0.89; hence, the pretreated CNTs contain more defects than the original CNTs, whose surfaces can facilitate loading metal particles. With increasing Ni content, the R values of the supported samples range from 0.84 to 0.90, which are lower than those of the pretreated CNTs. These results indicate that the loaded metal particles occupied the defects on the surface of CNTs decreasing amount of defects. However, increase Fe loading slightly increased the number of defects.

Therefore, in situ XPS and HS-LEIS characterizations show that several species, such as Ni–Fe alloys and Fe oxides, present on the surface of catalysts, and Fe species preferentially segregate on the surface of particles. The results of XRD, TPR, and STEM analyses reveal the formation of Ni–Fe alloys assignable to $Fe_1$–$Ni_3$ structure. In addition, it can be observed that the nanoparticle size decreases with decrease of Ni/Fe atomic ratio, which suggests that Fe promotes the dispersion of Ni.

### *3.2. HDO of guaiacol*

Initially, the catalytic performance of guaiacol HDO was evaluated over Ni catalysts supported on different carbon materials at 573 K and 3.0 MPa (Table S3). Of all carbon materials used, CNTs-supported catalyst is the optimal one for the guaiacol HDO reaction. The as-received CNTs show a negligible activity of 0.5% conversion at 573 K, and the purified CNTs display no activity. The superior catalytic results are obtained over the Ni–Fe/CNT catalysts in comparison with Ni/CNT and Fe/CNT, presumably due to the integrating properties of bimetals and CNTs for enhancing the absorption and activation of reactants. In all cases, the main C1 products are methane and methanol (Figure 5, the upper columns) while catechol, the product of demethylation, was not detected by FID. In this study, 2-methoxycyclohexanol is not detected, demonstrating that demethylation and demethoxylation occurr prior to the hydrogenation of aromatic rings. Additionally, products through aromatic ring condensation are detected by GC-MS in liquid phase. Only trace amounts of transalkylation products like cresols are detected, indicating that transalkylation reaction is negligible under present conditions. However, these products and other unknown products are classified as “Others” in the tables.

#### *3.2.1. Effect of Ni/Fe atomic ratio*

Figure 5 shows the effect of Ni/Fe atomic ratio on the catalytic performance.

Monometallic Ni/CNT demonstrates a high conversion activity of 79.0% but poor selectivity, meaning that the reaction pathways for the different products are energetically similar. The major C6 ring products include cyclohexane and cyclohexanol, while phenol and “Others” are also observed over Ni/CNT catalyst. Previous reports indicated that Ni can efficiently dissociate $H_2$, which is used as active metal in hydrogenation of aromatic rings [43,52]. Hence, hydrogenation of aromatic rings during guaiacol conversion easily occurs after demethylation and demethoxylation over the Ni/CNT catalysts. However, the Fe/CNT catalyst shows lower catalytic activity than Ni/CNT, affording phenol as the major product in C6 ring aromatics and many unknown products classified as “Others”, in contrast to the Ni-based catalysts. Therefore, Fe species demonstrates poor performance in guaiacol HDO. Similarly, Olcese et al. [26] reported that Fe/$SiO_2$ demonstrated deoxygenation activity without saturation of aromatic rings during conversion of guaiacol. However, the conversion of guaiacol and the selectivity to cyclohexane are promoted significantly upon introduction of a small amount of Fe into the catalysts studied. The selectivity to cyclohexane presented a volcano curve with decreasing Ni/Fe atomic ratio. The $Ni_5$–$Fe_1$/CNT catalyst shows higher selectivity to cyclohexane and conversion of 83.4% and 96.8%, respectively, compared with the other catalysts (Figure 5). This result indicates that the synergistic effect of bimetallic Ni–Fe catalysts promotes the performance of HDO facilitating a reaction mechanism. The synergy between Ni and Fe is commonly observable, Sitthisa et al. [50] investigated the possible adsorption of furfural on the surface of Ni(111) and Ni–Fe(111) alloy through DFT calculations. The furan ring is preferentially adsorbed on the surface of the Fe domain because of its oxophilic nature.

The strong interaction between Ni–Fe and furfural resulted in satisfactory conversion and selectivity. Sun et al. [30] studied the adsorption energies of phenol on the surface of Pd–Fe alloy through DFT calculations and revealed that Fe species favorably adsorbed phenol and weakened the C–O bond. Furthermore, the conversion and selectivity to C6 ring products decrease with decreasing Ni/Fe atomic ratio. The conversion of guaiacol and the selectivity to cyclohexane over the $Ni_2$–$Fe_1$/CNT catalyst are 85.0% and 78.7%, respectively. For the $Ni_1$–$Fe_1$/CNT catalyst in our case, the reaction shows a conversion of 75.0% and a cyclohexane selectivity of 39.1%. Apparently, addition of suitable Fe content enhanced the HDO of guaiacol. This phenomenon can be due to the fact that the HDO of guaiacol requires dissociation of $H_2$ on Ni species and adsorption of the O species of the substrate on Fe species to induce the cleavage of the C–O bond, corresponding to the TOF values summarized in Table 2. The amount of Ni species on the surface decrease with decreasing Ni/Fe atomic ratio (the total metal loading was maintained at 7 wt. %), thereby reducing the number of active sites for hydrogen activation. Hence, the activated hydrogen atoms are considered insufficient for hydrogenolysis of C–O bond and hydrogenation of aromatic rings. Other catalysts were also evaluated by maintaining the Ni loading constant at 7 wt. % but varying Fe content (Table S4). When Fe was introduced into the Ni/CNT, the conversion increased from 79.0% to 100.0% with incremental increase in Fe content. The selectivity to cyclohexane increased at large increments from 53.0% to 89.2%, supporting our explanation above.

To investigate whether the formation of Ni–Fe alloy resulted in high conversion and selectivity, we designed a control experiment by physical mixing of Ni/CNT and Fe/CNT

(Ni/Fe = 5/1) for forming a contrastive catalyst (Figure 5-h). The conversion is 69.0%, which is lower than that of $Ni_5$–$Fe_1$/CNT and $Ni_2$–$Fe_1$/CNT; moreover, the product distribution differs between the samples. The main C6 ring product is cyclohexanol, which demonstrates a selectivity of 55.9%. This result indicates that improvement in catalytic activity over Ni–Fe/CNT is mainly ascribed to the formation of Ni–Fe alloys, as proven by XRD, TEM, and other characterization techniques.

The conversion of guaiacol and the selectivity to phenol over the $Ni_1$–$Fe_5$/CNT increased compared with that of Fe/CNT. The $Ni_1$–$Fe_5$/CNT catalyst shows an incremental conversion of 47.2% and a phenol selectivity of 82.3%. The main C6 ring product of the reaction over Fe-based catalysts is phenol, in contrast with that of the reaction over Ni-based catalysts with saturation of aromatic rings. Fe demonstrates strong affinity to O but weak ability to adsorb and activate $H_2$. Thus, the preferred reaction is the hydrogenolysis of the $C_{aryl}$–$OCH_3$ bond over the Fe-based catalysts as the thermodynamic profile in Figure 6 indicates. Addition of small quantity of Ni increased the conversion of guaiacol and the selectivity to phenol as shown by the lower intermediate energy in $C_{aryl}$–$OCH_3$ scission mechanism on the $Fe_3Ni(111)$ energy profile. Hence, activation of hydrogen on the Ni surface is a necessary step to hydrogenolyze $C_{aryl}$–$OCH_3$ bonds. When the amount of Ni is adequate, phenol as the intermediate will further react with activated hydrogen, thereby increasing the amount of cyclohexanol and cyclohexane with increasing guaiacol conversion. Suitable Ni contents obviously increase the yield of phenol.

Given that $Ni_5$–$Fe_1$/CNT and $Ni_1$–$Fe_5$/CNT exhibited high selectivity to cyclohexane and phenol, respectively, we investigated the effects of WLHSV. Figure 8-a shows the effect of WLHSV on the performance of the $Ni_5$–$Fe_1$/CNT catalyst. The conversion and selectivity to cyclohexane increased from 58.9% to 99.8% and from 49.0% to 99.9%, respectively, as the WLHSV decreased from 12 to 3. The amount of cyclohexanol, as the major by-product, decreased with decreasing WLHSV; hence, cyclohexane was formed from cyclohexanol through the hydrogenolysis of the $C_{alkyl}$–OH bond. This result indicates that cyclohexanol, as an intermediate, reacts easily with $H_2$ as increasing residence time on the active sites, resulting in increased amount of cyclohexane. $Ni_1$–$Fe_5$/CNT performs lower activity than the $Ni_5$–$Fe_1$/CNT catalyst (Figure 8-b). At high WLHSV (10 $h^{-1}$), the conversion is calculated as 22.1% with 65% selectivity of phenol. The “Others” are mainly M-cresol and P-cresol, which are identified through GC-MS and FID detector. Over the $Ni_1$–$Fe_5$/CNT catalyst, with decreasing WLHSV, the conversion and selectivity to phenol increase from 22.1% to 62.7% and from 64.9% to 83.7%, respectively, whereas the selectivity to “Others” decrease obviously. These findings suggest that decreased WLHSV, which corresponds to increase in residence time on the surface of the catalysts, the guaiacol reacts with $H_2$ adequately to form phenol with high selectivity.

It is known that not only catalytic properties but chemical stability of monometallic active phase can be significantly promoted through adding second metal to form bimetallic nanoparticles. Figure 9-a–b shows the conversion and the selectivity over on Ni–Fe catalysts as a function of time. For monometallic Ni/CNT, the initial conversion is approximately 80% and displays a rapid deactivation after 5 h. The decrease of selectivity to cyclohexane and cyclohexanol reveal the disappearance of HDO ability. Whereas, both bimetallic $Ni_5$–$Fe_1$/CNT and $Ni_1$–$Fe_5$/CNT show promoted stabilities without noticeable deactivation; the selectivity to cyclohexane and phenol slightly fluctuate the initial selectivities. XRD patterns and TEM images of fresh and spent catalysts (Figures S9 and S10) reveal that bimetallic nanoparticles showed less sintering in contrast to that of monometallic Ni/CNT and formed thermodynamically stable alloy structure which is presumable that cohesive energy decrease with the incorporation of Fe in agreement with previous reports [42,53].

Briefly, the results demonstrate the good performance of bimetallic Ni–Fe/CNT catalysts on the HDO and hydrogenolysis of guaiacol. Variation in Ni/Fe atomic ratios remarkably changes the distribution of products, resulting in tunable selectivity to phenol and cyclohexane. When the major domain is Ni species, the main products of the hydrogenation of aromatic rings include cyclohexanol and cyclohexane. The yield of cyclohexane peaks over the $Ni_5$–$Fe_1$/CNT catalyst. The formation of Ni–Fe alloys also enhances the selectivity to cyclohexane. In addition, the reaction over the Fe-based catalysts produces phenol as the major product, and the selectivity to phenol peaked at the Ni/Fe atomic ratio of 0.2. Nonetheless, the HDO performance is inevitably related to the bimetallic particle size and reduction extent of Ni–Fe/CNT catalysts.

### *3.2.2. Effects of Ni–Fe nanoparticle size and reduction extent*

To investigate the effects of Ni–Fe nanoparticle size and phase change on the HDO of guaiacol, we prepared a series of catalysts with different reduction temperatures and evaluated their HDO performances under identical conditions (Table 2). Entries 1–3 in Table 2 show the performances for HDO of guaiacol over Ni/CNT, which was reduced at

673 K, 773 K, and 873 K, respectively. The conversion slightly fluctuates within 77%–81%; however, the selectivity to cyclohexane decreases sharply from 53.0% to 4.6%, and the selectivity to cyclohexanol increases from 31.7% to 69.7%. Moreover, the selectivity to phenol over Entry 3 rapidly increases and reaches 10.4%. To try to make a possible discrimination of the influences of metallic particle size and its chemical state on the catalyst performance, XPS measurements of Ni/CNT catalyst reduced at different temperatures were carried out and the results are showed in Figure S11 and Table S5. It can be seen that the surface $Ni^0$ concentration increase from 31.1% to 43.3% with the increase of metallic particle sizes from 9.2 nm to 16.0 nm. However, the catalytic performances decrease clearly even if the extent of reduction increase, suggesting that the metallic particles size is the main factor that influences the catalytic performance in comparison with the nature of nanoparticles on the catalyst surface. This phenomenon reveals that reaction activity of the catalyst decreases with increasing metallic particle size, resulting in reduced ability for hydrogenation of aromatic rings and hydrogenolysis of $C_{alkyl}$–OH bonds. These results are consistent with those of previous studies, which showed that small metal particles are beneficial for hydrogenation reactions, whereas large particles and bulks can weakly activate hydrogen [54,55].

The performance tendency of $Ni_5$–$Fe_1$/CNT catalysts from Entries 4–6 is similar to that over monometallic Ni/CNT catalysts. The selectivity to cyclohexane rapidly decreases and the selectivity to cyclohexanol increases with increasing reduction temperature, indicating a decline of catalytic performance. The XPS results (Figure S12 and Table S6) show that the surface $Ni^0$ concentration has a slight increase from 38.0% to 44.3% while the $Fe^0$ concentration increases greatly from 9.1% to 26% with the increase of reduction temperature. In this case, the metallic particle sizes increase from 7.7 nm to 11.2 nm. Therefore, the metallic particles size is considered as one of the crucial factors that influence the catalytic performance, particularly in diversity of product distribution. Furthermore, comparison of activity between Ni/CNT and $Ni_5$–$Fe_1$/CNT indicates that the bimetallic $Ni_5$–$Fe_1$/CNT catalysts always display smaller metallic particle size and improved performance than Ni/CNT catalysts at the same reduction temperature. This finding reveals that addition of Fe species enable improved dispersion of nanoparticle and promote hydrogenolysis of $C_{alkyl}$–OH bonds. Compared with that of Ni-based catalysts, the metallic particle size of Fe-based catalysts shows less sensitivity to reduction temperature. Entries 7–9 for $Ni_1$–$Fe_5$/CNT catalyst reduced at 673 K, 773 K, and 873 K exhibit similar particle sizes and present similar HDO performance. The main product is phenol, and the conversion and selectivity are approximately 40%–50% and 80%, respectively. The by-product cyclohexanol is also observed, indicating that a competitive relationship existed between cleavage of $C_{aryl}$–$OCH_3$ bond and hydrogenation of phenol. For the Fe/CNT catalysts, Entry 11 shows improved performance than Entry 10, despite their similar metallic particle sizes; hence, $Fe^0$ species is beneficial for hydrogenolysis of guaiacol. The catalyst of Entry 12 with a particle size of 11.5 nm displays weak activity. Thus, a small metallic particle is preferred for cleavage of C–O bonds and HDO of guaiacol.

To better understand the essence of Ni–Fe nanoparticles on the catalytic behaviour, the TOF values based on the metal dispersions (Table S7) by particle size estimated by

TEM and XRD were calculated and the results are summarized in Table 2. Ni/CNT catalyst with different reduction temperatures (Entry 1–3) exhibits similar TOF values but quite different product distributions, indicating that in addition to the simple relationship between the amount of surface metal atoms and the catalytic activity, particle size effect also exists on the formation of catalytic sites with hydrogenation of aromatic ring and hydrogenolysis of C–O bond. The different distributions of products suggest that the conversion of guaiacol is a structure-sensitive reaction. Mortensen [56] et al. observed a strong influence of nickel particle size on HDO of phenol and suggested that the large particles are very active for hydrogenation of aromatic ring while small particles are required to facilitate deoxygenation; it is consistent with our results. Compared with Ni/CNT catalyst, $Ni_5$–$Fe_1$/CNT catalyst (Entry 4–6) performs higher TOF value and better selectivity to deoxygenation products, which is ascribed to modification of Fe to the surface of nanoparticles. The decline of TOF values with the increase of reduction temperature and the diversity of product distribution indicate that the metallic particles size is the significant factor that influences the HDO of guaiacol.

To summarize, the effect of nanoparticle size and reduction extent caused by different reduction temperatures truly influence the catalytic activity and selectivity. The particle size effect shows a more significant influence in comparison with the phase change of nanoparticles. Therefore, the performance of guaiacol HDO over the bimetallic Ni–Fe catalysts can be tuned through variations of metal nanoparticle size and reduction extent in addition to the Ni/Fe atomic ratio.

### *3.2.3. HDO network of guaiacol over Ni–Fe/CNT catalysts*

Several reaction networks for HDO of guaiacol have been proposed to elucidate the reaction pathways over different catalysts [2,6,13]. Demethylation and demethoxylation are proposed to be the first step in reaction pathways. In many cases, methane is the by-product of demethylation over various catalysts, such as Ru/MgO, Ru/C, and Fe/$SiO_2$ [11,19,26]. Previous studies reported that demethylation occurred on activated metal sites, and methyl group remained on the surface [6,57]. As an alternative pathway, methanol and phenol are formed through the cleavage of $C_{aryl}$–$OCH_3$, which explains the presence of $CH_3OH$. The demethoxylation reaction is observed over several catalysts, such as sulfided Co–Mo/$Al_2O_3$, Co–Mo/$ZrO_2$, and supported $Ni_2P$. Phenol can be deoxygenated to obtain completely deoxygenated products. However, the conversion of phenol proceeds in different pathways, depending on the activated species of catalysts. Studies show that the hydrogenation of the aromatic ring occurs before dehydroxylation of phenol over many catalysts [6,13,58]. Moreover, transalkylation occurs during HDO of guaiacol, especially on Lewis acidic catalysts [21,22]. Consequently, different products (i.e., phenol, benzene, cyclohexanol, cyclohexane, and catechol) can be obtained by controlling the reaction pathways over different catalysts.

Scheme 1 illustrates the proposed pathways of CNT-supported Ni–Fe bimetallic catalyst used in this study. Methane and methanol are observed as C1 by-products during the HDO of guaiacol over Ni–Fe bimetallic catalysts, indicating that both demethylation and demethoxylation occurr in the reaction. However, no catechol is detected in all cases, suggesting that this compound is rapidly deoxygenated into phenol. In addition, we introduced pure methanol to the reactor as a blank test and observed the production of methane. That is to say, methane can also be derived from the $CH_3OH$ reduction. Phenol is the major intermediate formed from demethoxylation of guaiacol. Phenol can further react to yield products with saturated rings in some catalysts, such as Ni/CNT and $Ni_5$–$Fe_1$/CNT. Consistent with data presented in Figure 5, trace benzene is observed, and products with saturated rings (cyclohexanol and cyclohexane) are found to be the major products. Furthermore, cyclohexene and the products of aromatic rings are observed by analyzing the mixture collected through condensation by using GC-MS (Figure S13). Table S8 also shows the conversion of phenol as the intermediate compound at which case that cyclohexanon and cyclohexanol could be observed. These results suggest that phenol hydrogenation occurr before the cleavage of the last $C_{aryl}$–OH. Cyclohexanol can be further deoxygenated when suitable Fe contents were introduced.

To elucidate the synergism of Ni–Fe nanoparticles for HDO of guaiacol over Ni–Fe bimetallic catalysts containing various Ni/Fe atomic ratios, we propose appropriate reaction mechanisms in Scheme 2. Our results show that saturation of aromatic rings over monometallic Ni/CNT catalyst is favored to produce cyclohexanol and cyclohexane. As depicted in Scheme 2-a, Ni demonstrates high hydrogen absorption and activation abilities but weak substrate absorption. After demethoxylation of guaiacol, phenol can be adsorbed plainly on the Ni surface and then react with activated hydrogen to form cyclohexanol. However, cyclohexanol can hardly further react to yield cyclohexane because of weak oxygen affinity, causing low selectivity to cyclohexane. When suitable Fe contents are introduced into the surface of Ni, the HDO ability of catalyst is considerably enhanced, as shown in Scheme 2-b. Compared with Ni species, Fe demonstrates strong activation of the molecule, though the binding is weaker by 48.24 kJ mol$^{-1}$. On the surface of Ni–Fe nanoparticles, Fe sites stabilize intermediates, while Ni sites favor the adsorption of activated hydrogen. This behavior was also observed in Pd–Fe catalysts, in which Fe is likely the active site for HDO of phenol. Figure 5 shows that the selectivity to cyclohexanol and phenol increased when the Ni/Fe atomic ratios are lower than 2. This phenomenon reveals that further hydrogenation and hydrogenolysis of the $C_{alkyl}$–OH bond require a sufficient amount of activated hydrogen on the surface of Ni, as proven by the result of additional experiments (Table 3). Scheme 2-c shows a proper reaction pathway on the surface of the Fe/CNT catalyst. Some activated substrates reacted with hydrogen to yield phenol, whereas other substrates occurred by-reaction such as oligomerization to form by-products unrecognized in the absence of sufficient amounts of activated hydrogen. In the case of $Ni_1$–$Fe_5$/CNT as described in Scheme 2-d, when a small amount of Ni is introduced into Fe surface, the dissociation of $H_2$ greatly enhances, thereby increasing the selectivity to phenol.

The enhanced effect for HDO of guaiacol can be due to the synergism between Ni and Fe species. Ni promotes dissociation of $H_2$, whereas Fe plays a crucial role in oxygen affinity. Different amounts of Ni and Fe in the catalysts remarkably change the distribution of products. High selectivity to cyclohexane and phenol can be obtained by controlling the content of Ni and Fe, an approach that is easy to operate.

## 4. Conclusions

In summary, non-precious Ni–Fe/CNT catalysts have been investigated for the efficient HDO of guaiacol. Product distribution is readily tuned by changing the Ni/Fe atomic ratios, which can obtain 99.8% selectivity to cyclohexane and 83.7% selectivity to phenol over the Ni–Fe/CNT catalysts with Ni/Fe atomic ratios of 5/1 and 1/5, respectively, under suitable conditions. A plausible reaction mechanism is proposed to explain the results over the Ni–Fe bimetallic catalysts. The enhanced effects are attributed to the strong interactions of Ni and Fe in addition to the effect of support. The formation of Ni–Fe alloys is evidenced by using TPR, XRD, and STEM analyses. The Fe and Ni species on the surface of Ni–Fe particles, which demonstrate strong π-system activation, i.e. aromatic ring, and high ability to dissociate $H_2$, exert the synergistic effects to enhance the HDO of guaiacol. Further results reveal that the performance of guaiacol HDO also depends on the chemical state and size of the metallic nanoparticles in addition to the Ni/Fe atomic ratio. The metallic particle size considerably influences the catalytic activity, in particularly the product selectivity. Smaller metallic particles perform higher hydrogenolysis activity of C–O bonds while larger metallic particles show lower catalytic activity. We conclude that the appropriate combination of Ni and Fe with fine control of metallic particle size is necessary for the optimal HDO of guaiacol to obtain high selectivity to cyclohexane or phenol.

## Acknowledgements

We acknowledge the financial support from the Natural Science Foundation of China (21303141, 21403178, 21473145 and 91545115), and the Program for Innovative

Research Team in Chinese Universities (No. IRT_14R31). The authors also acknowledge the use of the Advanced Research Computing @ Cardiff (ARCCA) at Cardiff University, and associated support services.

## References

[1] A. J. Ragauskas, C. K. Williams, B. H. Davison, G. Britovsek, J. Cairney, C. A. Eckert, W. J. Frederick Jr., J. P. Hallett, D. J. Leak, C. L. Liotta, J. R. Mielenz, R. Murphy, R. Templer, T. Tschaplinski, Science, 311 (2006) 484–489.

[2] J. Zakzeski, P. C. A. Bruijinincx, A. L. Jongerius, B. M. Weckhuysen, Chem. Rev., 110 (2010) 3552–3599.

[3] G. W. Huber, S. Iborra, A. Corma, Chem. Rev., 106 (2006) 4044–4098.

[4] C. Li, X. Zhao, A. Wang, G. W. Huber, T. Zhang, Chem. Rev., 115 (2015) 11559–11624.

[5] J. C. Serrano-Ruiz, J. A. Dumesic, Energ. Environ. Sci., 4 (2011) 83–99.

[6] M. Saidi, F. Samimi, D. Karimipourfard, T. Nimmanwudipong, B. C. Gates, M. R. Rahimpour, Energ. Environ. Sci., 7 (2014) 103–129.

[7] J. E. Holladay, J. J. Bozell, J. F. White, D. Johnson, Report PNNL, (2007).

[8] R. Rinaldi, F. Schüth, Energ. Environ. Sci., 2 (2009) 610–626.

[9] I. Graça, J. M. Lopes, M. F. Ribeiro, F. Ramôa Ribeiro, H. S. Cerqueira, M. B. B. de Almeida, Appl. Catal. B-Environ., 101 (2011) 613–621.

[10] P. R. Patwardhan, R. C. Brown, B. H. Shanks, ChemSusChem, 4 (2011) 1629–1636.

[11] Y. Nakagawa, M. Ishikawa, M. Tamura, K. Tomishige, Green Chem., 16 (2014) 2197–2203.

[12] S. K. Wu, P. C. Lai, Y. C. Lin, H. P. Wan, H. T. Lee, Y. H. Chang, ACS Sustain. Chem. Eng., 1 (2013) 349–358.

[13] Y. K. Hong, D. W. Lee, H. J. Eom, K. Y. Lee, Appl. Catal. B-Environ., 150–151 (2014) 438–445.

[14] A. Centeno, E. Laurent, B. Delmon, J. Catal., 154 (1995) 288–298.

[15] A. L. Jongerius, R. Jastrzebski, P. C. A. Bruijnincx, B. M. Weckhuysen, J. Catal., 285 (2012) 315–323.

[16] M. Badawi, J. F. Paul, S. Cristol, E. Payen, Y. Romero, F. Richard, S. Brunet, D. Lambert, X. Portier, A. Popov, E. Kondratieva, J. M. Goupil, J. El Fallah, J. P. Gilson, L. Mariey, A. Travert, F. Maugé, J. Catal., 282 (2011) 155–164.

[17] X. L. Ma, K. Sakanishi, I. Mochida, Ind. Eng. Chem. Res., 33 (1994) 218–222.

[18] O. İ. Şenol, T. R. Viljava, A. O. I. Krause, Appl. Catal. A-Gen., 326 (2007) 236–244.

[19] A. Sanna, T. P. Vispute, G. W. Huber, Appl. Catal. B-Environ., 165 (2015) 446–456.

[20] X. Zhu, L. L. Lobban, R. G. Mallinson, D. E. Resasco, J. Catal., 281 (2011) 21–29.

[21] T. Nimmanwudipong, C. Aydin, J. Lu, R. C. Runnebaum, K. C. Brodwater, N. D. Browning, D. E. Block, B. C. Gates, Catal. Lett., 142 (2012) 1190–1196.

[22] T. Nimmanwudipong, R. C. Runnebaum, D. E. Block, B. C. Gates, Energ. Fuel, 25 (2011) 3417–3427.

[23] D. Gao, C. Schweitzer, H. T. Hwang, A. Varma, Ind. Eng. Chem. Res., 53 (2014) 18658–18667.

[24] X. Zhang, T. Wang, L. Ma, Q. Zhang, Y. Yu, Q. Liu, Catal. Commun., 33 (2013) 15–19.

[25] R. Olcese, M. M. Bettahar, B. Malaman, J. Ghanbaja, L. Tibavizco, D. Petitjean, A. Dufour, Appl. Catal. B-Environ., 129 (2013) 528–538.

[26] R. N. Olcese, M. Bettahar, D. Petitjean, B. Malaman, F. Giovanella, A. Dufour, Appl. Catal. B-Environ., 115-116 (2012) 63–73.

[27] W. Song, Y. Liu, E. Baráth, C. Zhao, J. A. Lercher, Green Chem., 17 (2015) 1204–1218.

[28] A. R. Ardiyanti, S. A. Khromova, R. H. Venderbosch, V. A. Yakovlev, H. J. Heeres, Appl. Catal. B-Environ., 117–118 (2012) 105–117.

[29] A. B. Dongil, L. Pastor-Pérez, A. Sepúlveda-Escribano, R. García, N. Escalona, Fuel, 172 (2016) 65–69.

[30] J. Sun, A. M. Karim, H. Zhang, L. Kovarik, X. S. Li, A. J. Hensley, J. S. McEwen, Y. Wang, J. Catal., 306 (2013) 47–57.

[31] P. Luksirikul, K. Tedsree, M. G. Moloney, M. L. Green, S. C. Tsang, Angew. Chem. Int. Ed., 51 (2012) 6998–7001.

[32] P. Zhang, C. L. Shao, Z. Y. Zhang. M. Y. Zhang, J. B. Mu, Z. C. Guo, Y. C. Liu. Nanoscale 3 (2011) 3357–3363.

[33] G. Kresse, J. Hafner, Phys. Rev. B, 47 (1993) 558–561.

[34] G. Kresse, J. Furthmüller, Comput. Mat. Sci., 6 (1996) 15–50.

[35] N. D.Mermin, Phys. Rev., 137 (1965) 1441–1443.

[36] J. Perdew, A. Ruzsinszky, G. Csonka, O. Vydrov, G. Scuseria, L. Constantin, X.

Zhou, K.Burke, Phys. Rev. Lett., 100 (2008) 136406.

[37] S. Grimme, J. Comput. Chem., 27 (2006) 1787–1799.

[38] S. Irrera, A. Roldan, G. Portalone, N. H. de Leeuw, J. Phys. Chem. C, 117 (2013) 3949–3957.

[39] S. S. Tafreshi, A. Roldan, N. Y. Dzade, N. H. de Leeuw, Surf. Sci., 622 (2014) 1–8.

[40] N. Dzade,; A. Roldan, N. H. de Leeuw, Minerals, 4 (2014) 89–115.

[41] H. J. Monkhorst, J. D. Pack, Phys. Rev. B, 13 (1976) 5188–5192.

[42] X. Yu, J. Chen, T. Ren, RSC Adv., 4 (2014) 46427–46436.

[43] L. Nie, P. M. de Souza, F. B. Noronha, W. An, T. Sooknoi, D. E. Resasco, J. Mol. Catal. A-chem., 388–389 (2014) 47–55.

[44] A. B. Dongil, I. T. Ghampson, R. Garc´ıa, J. L. G. Fierro, N. Escalona. RSC Adv., 6 (2016) 2611–2623

[45] A. B. Dongil, B. Bachiller-Baeza, I. Rodr´ıguez-Ramos, J. L. G. Fierro, N. Escalona. RSC Adv., 6 (2016) 26658–26667

[46] B. Li, J. Wang, Y. Yuan, H. Ariga, S. Takakusagi, K. Asakura, ACS Catal., 1 (2011) 1521–1528.

[47] S. Leng, X. Wang, X. He, L. Liu, Y. E. Liu, X. Zhong, G. Zhuang, J. G. Wang, Catal. Commun., 41 (2013) 34–37.

[48] H. X. Yang, S. Q. Song, R. C. Rao, X. Z. Wang, Q. Yu, A. M. Zhang. J. Mol. Catal. A-chem., 1–2 (2010) 33–39.

[49] S. H. Lu, C. Zhang, Y. Liu. Int. J. Hydreogen Energ., 3 (2011) 1939–1948.

[50] S. Sitthisa, W. An, D. E. Resasco, J. Catal., 284 (2011) 90–101.

[51] A. Nieto-Márquez, S. Gil, A. Romero, J. L. Valverde, S. Gómez-Quero, M. A. Keane, Appl. Catal. A-Gen., 363 (2009) 188–198.

[52] H. Shafaghat, P. S. Rezaei, W. M. A. W. Daud. J. Ind. Eng. Chem., 35 (2016) 268–176.

[53] Y. Mishin, M. J. Mehl, D. A. Papaconstantopoulos. Acta Mater., 53 (2005) 4029–4041.

[54] J. H. Kima, D. J. Suh,T. J. Parkb, K. L. Kima, Appl. Catal. A-Gen., 197 (2000) 191–200.

[55] M. Ojeda, S. Rojas, M. Boutonnet, F. J. Pérez-Alonso, F. Javier García-García, J. L. G. Fierro, Appl. Catal. A-Gen., 274 (2004) 33–41.

[56] P. M. Mortensen, J. D. Grunwaldt, P. A. Jensen, A. D. Jensen. Catal. Today, 259 (2016) 277–284.

[57] L. Souza Macedo, D. R. Stellwagen, V. Teixeira da Silva, J. H. Bitter, ChemCatChem, 7 (2015) 2816–2823.

[58] Q. Tan, G. Wang, L. Nie, A. Dinse, C. Buda, J. Shabaker, D. E. Resasco, ACS Catal., 5 (2015) 6271–6283.

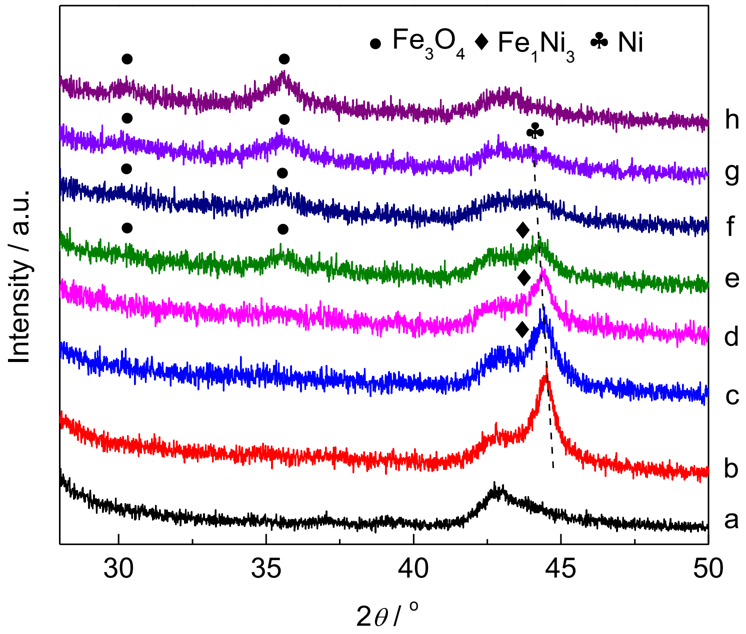

**Figure 1** XRD patterns of Ni–Fe/CNT catalysts with different Ni/Fe atomic ratios reduced at 673 K: (a) CNT, (b) Ni/CNT, (c) $Ni_5–Fe_1$/CNT, (d) $Ni_2–Fe_1$/CNT, (e) $Ni_1–Fe_1$/CNT, (f) $Ni_1–Fe_2$/CNT, (g) $Ni_1–Fe_5$/CNT, and (h) Fe/CNT.

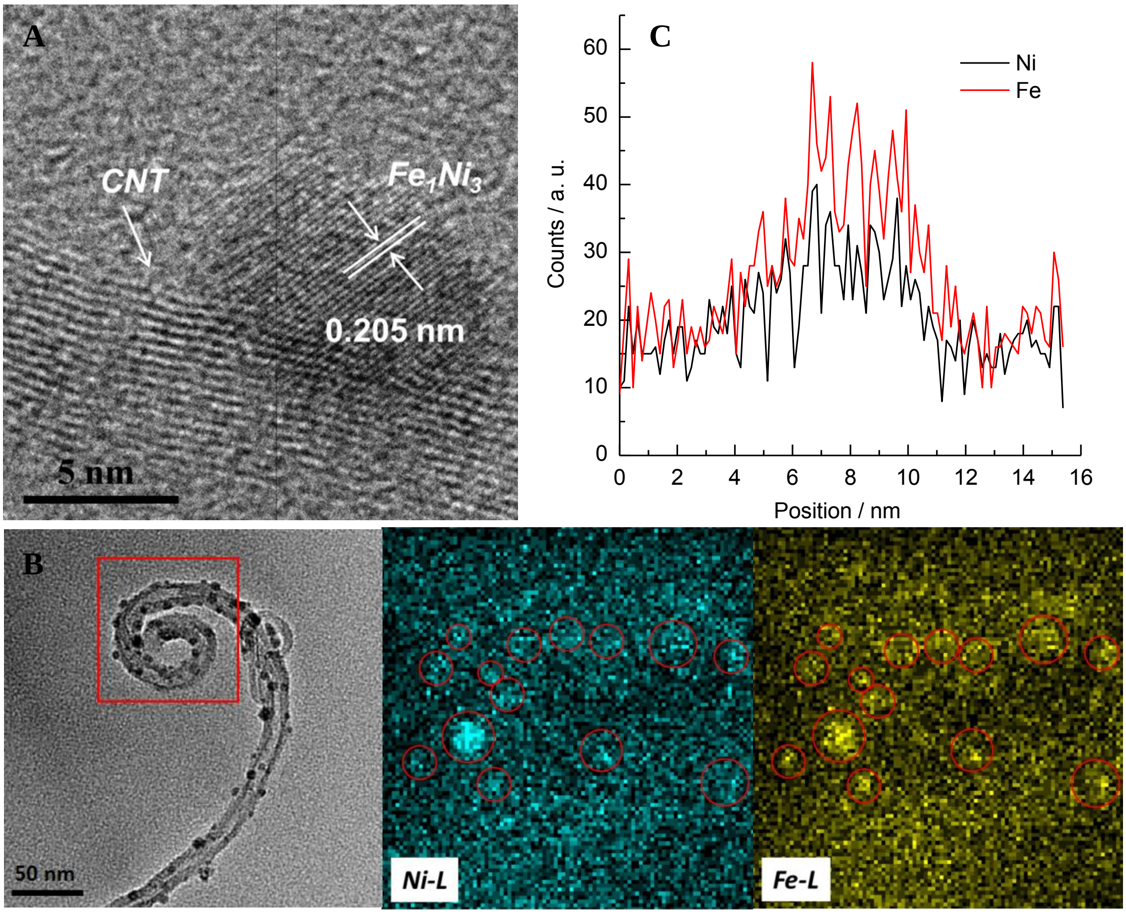

**Figure 2** **(A)** HRTEM image, **(B)** STEM-EDX mapping and **(C)** linear scanning of as-reduced $Ni_5$–$Fe_1$/CNT catalyst.

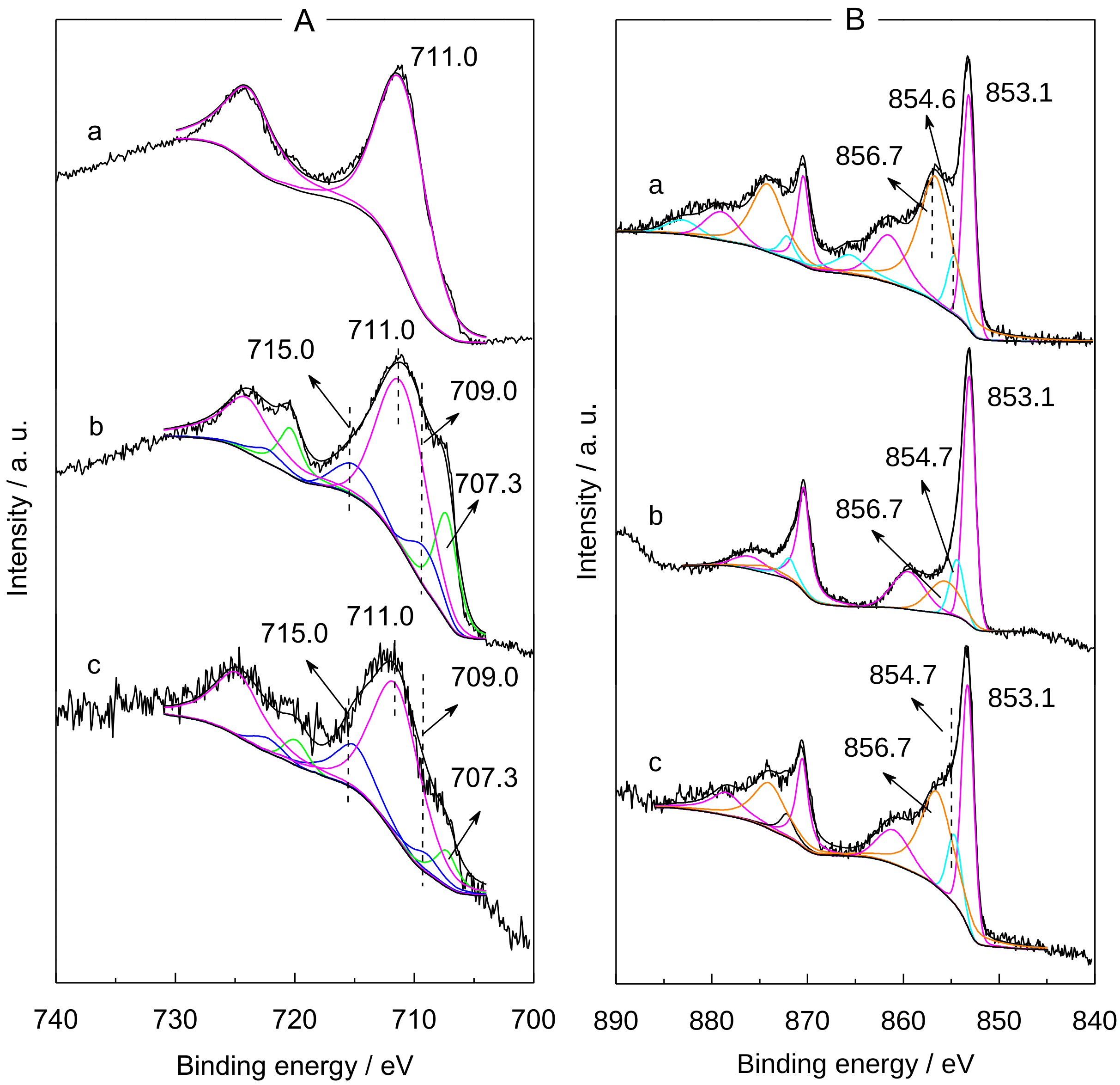

**Figure 3** **(A)** Fe 2p XPS profiles: (a) Fe/CNT, (b) $Ni_2$–$Fe_1$/CNT, and (c) $Ni_5$–$Fe_1$/CNT; **(B)** Ni 2p XPS profiles: (a) Ni/CNT, (b) $Ni_2$–$Fe_1$/CNT, and (c) $Ni_5$–$Fe_1$/CNT.

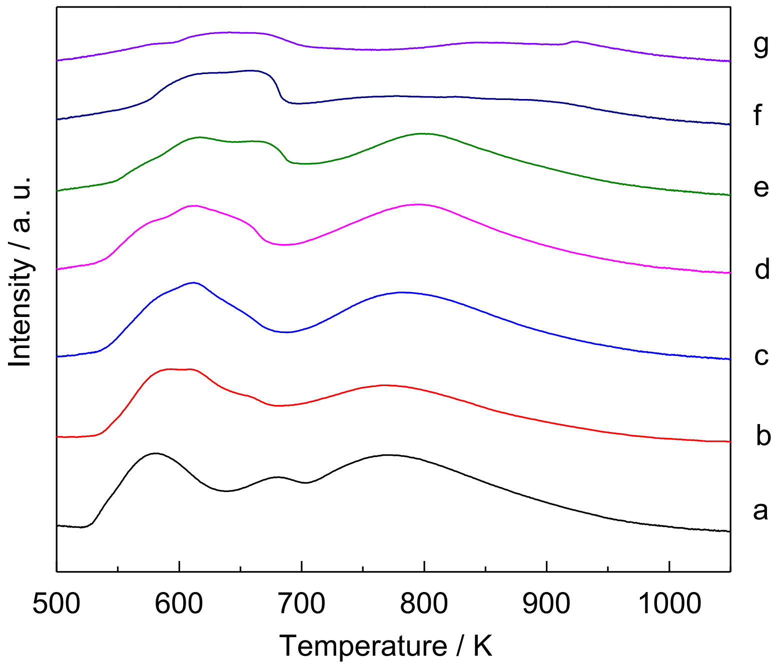

**Figure 4** $H_2$-TPR profiles of Ni–Fe/CNT catalysts with different Ni/Fe atomic ratios: (a) Ni/CNT, (b) $Ni_5$–$Fe_1$/CNT, (c) $Ni_2$–$Fe_1$/CNT, (d) $Ni_1$–$Fe_1$/CNT, (e) $Ni_1$–$Fe_2$/CNT, (f) $Ni_1$–$Fe_5$/CNT, and (g) Fe/CNT.

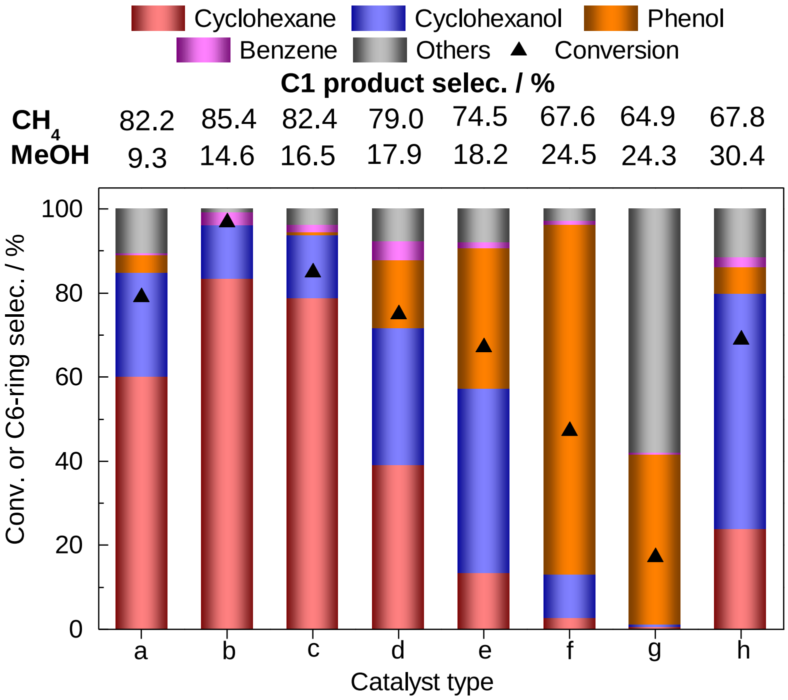

**Figure 5** Catalytic performances of Ni–Fe/CNT catalysts with different Ni/Fe atomic ratios: (a) Ni/CNT, (b) $Ni_5$–$Fe_1$/CNT, (c) $Ni_2$–$Fe_1$/CNT, (d) $Ni_1$–$Fe_1$/CNT, (e) $Ni_1$–$Fe_2$/CNT, (f) $Ni_1$–$Fe_5$/CNT, (g) Fe/CNT, and (h) Ni/CNT + Fe/CNT (Ni/Fe = 5/1). Reaction conditions: $WLHSV_{GUA}$= 6.0 $h^{-1}$, P ($H_2$)=3.0 MPa, $H_2$/GUA molar ratio = 50, $T$= 573 K.

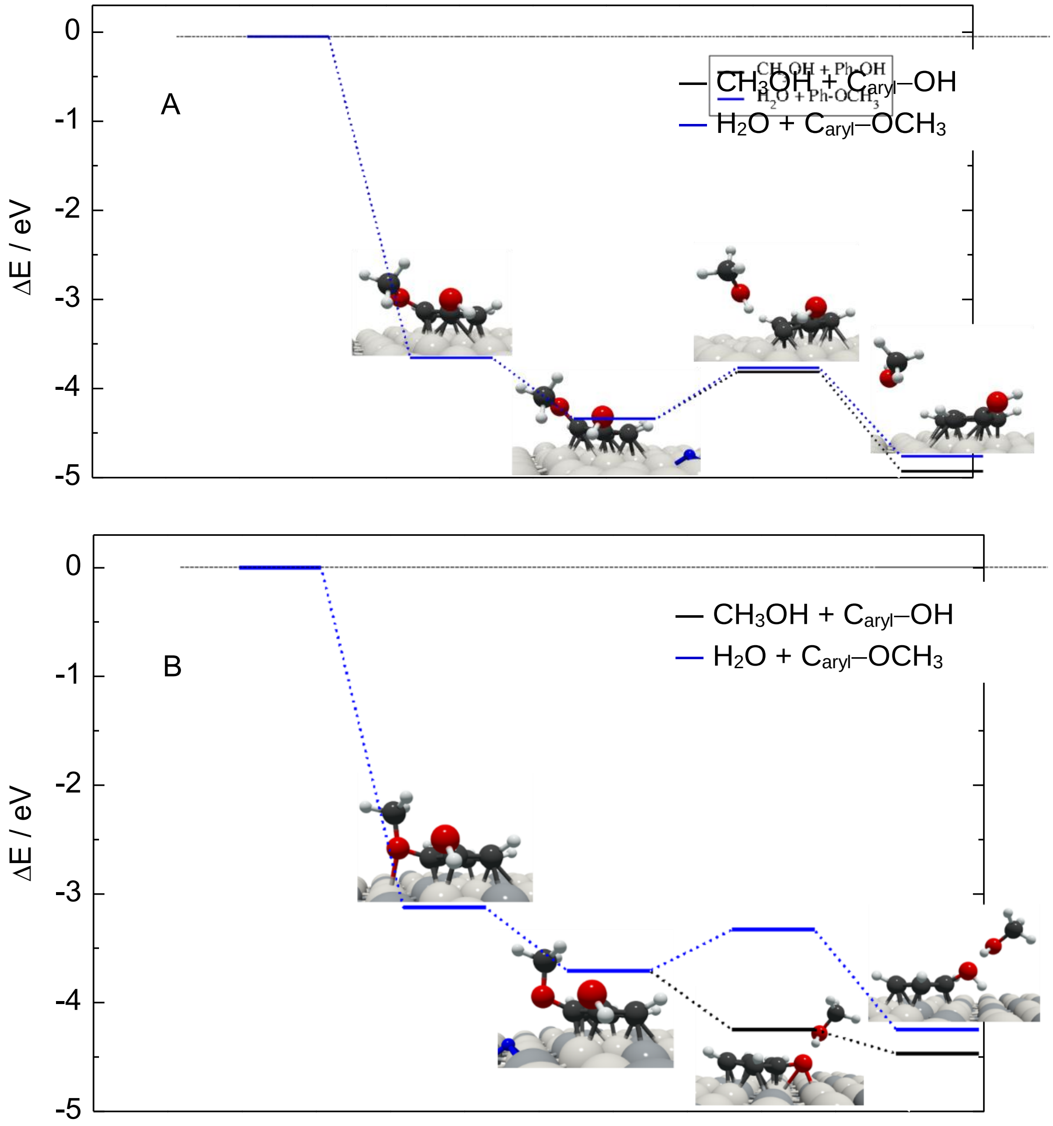

**Figure 6** Thermodynamic energy profile for guaiacol reduction on **(A)** pristine Ni(111) and **(B)** $Fe_3Ni(111)$ surfaces. Each state corresponds to a single hydrogenation step leading to $CH_3OH$ + $C_{aryl}$–OH (black line and representation insets) and $H_2O$ + $C_{aryl}$–$OCH_3$ (blue line). Color scheme: light-grey represents Ni, grey is Fe, dark grey is C, red is O white is H and the co-adsorbed H is represented in blue.

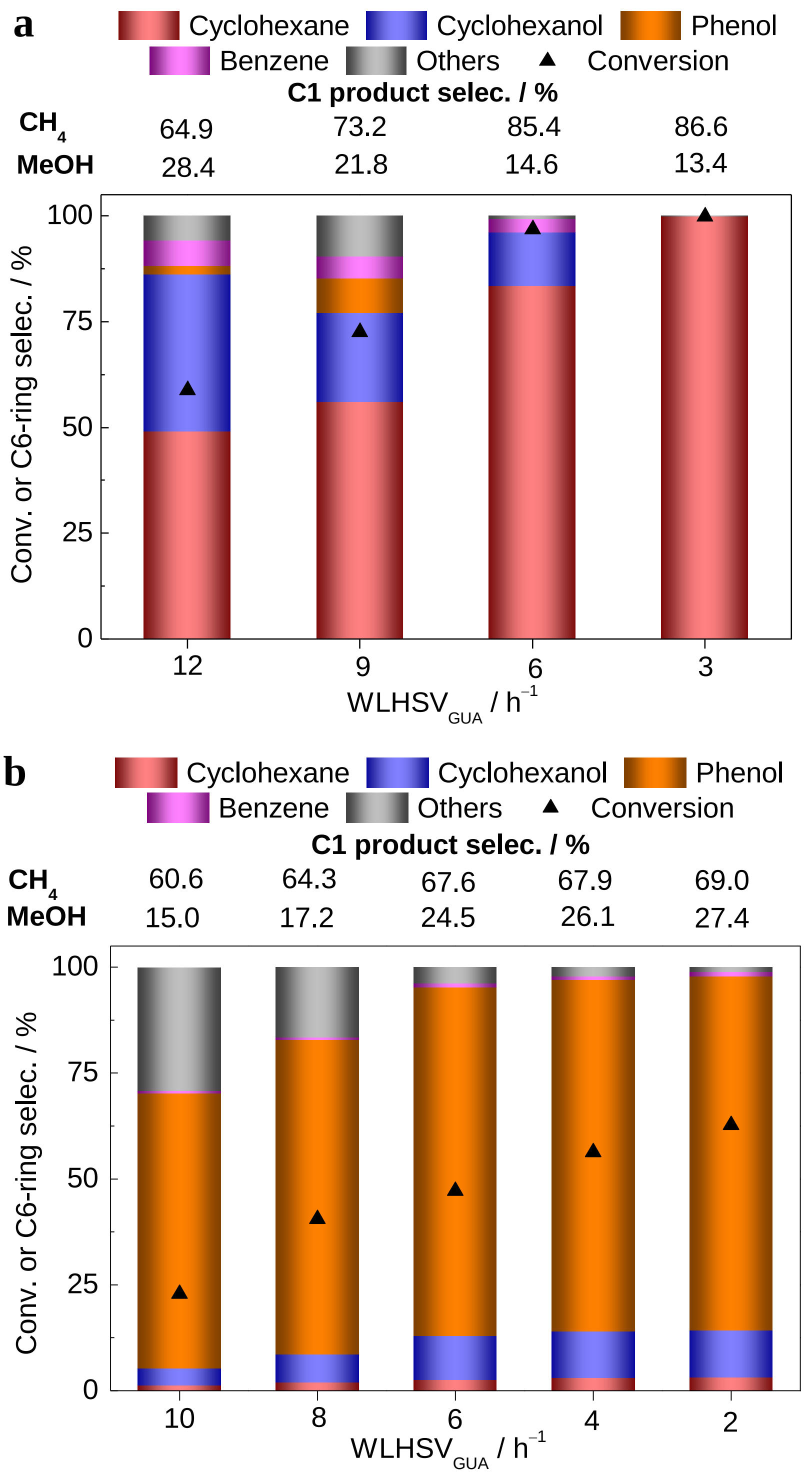

**Figure 7** Catalytic performances of catalysts (a) $Ni_5$–$Fe_1$/CNT and (b) $Ni_1$–$Fe_5$/CNT as a function of $WLHSV_{GUA}$. Other reaction conditions: P ($H_2$)=3.0 MPa, $H_2$/GUA molar ratio = 50, *T*= 573 K..

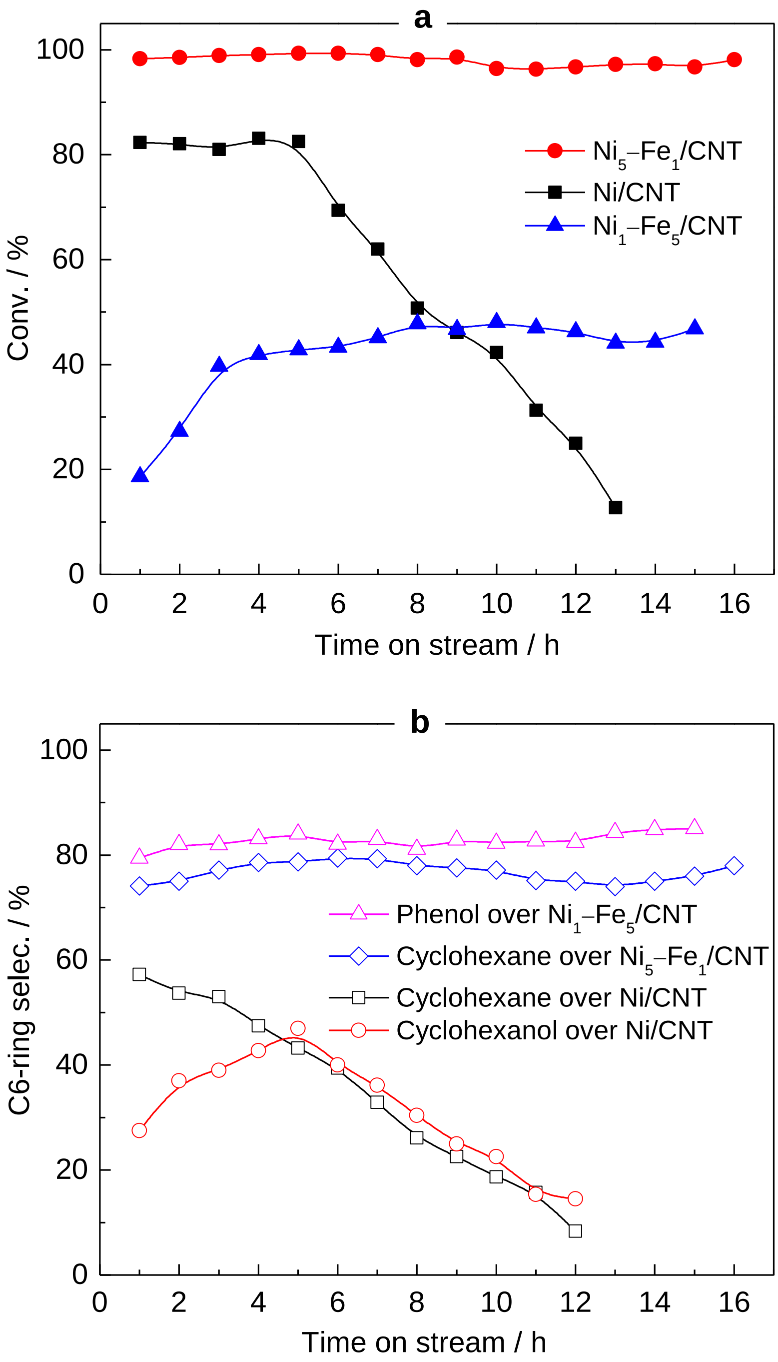

**Figure 8** Conversion (a) and selectivity (b) over catalysts Ni/CNT, $Ni_5$–$Fe_1$/CNT, and $Ni_1$–$Fe_5$/CNT as a function of time on stream. Reaction conditions: $WLHSV_{GUA} = 6.0\ h^{-1}$, P ($H_2$) = 3.0 MPa, $H_2$/GUA molar ratio = 50, $T = 573$ K.

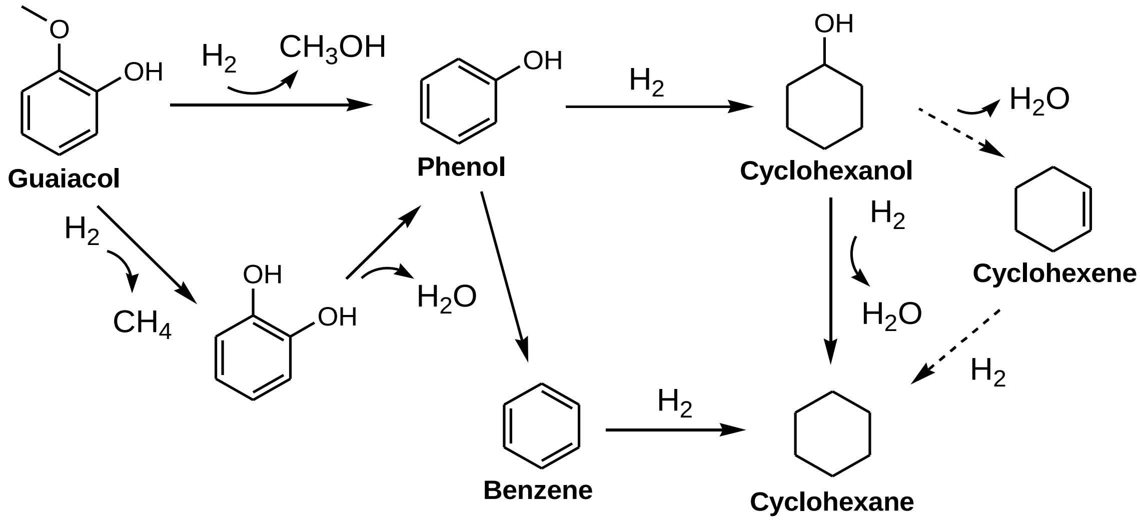

**Scheme 1** Reaction pathways for HDO of guaiacol on Ni−Fe/CNT bimetallic catalysts.

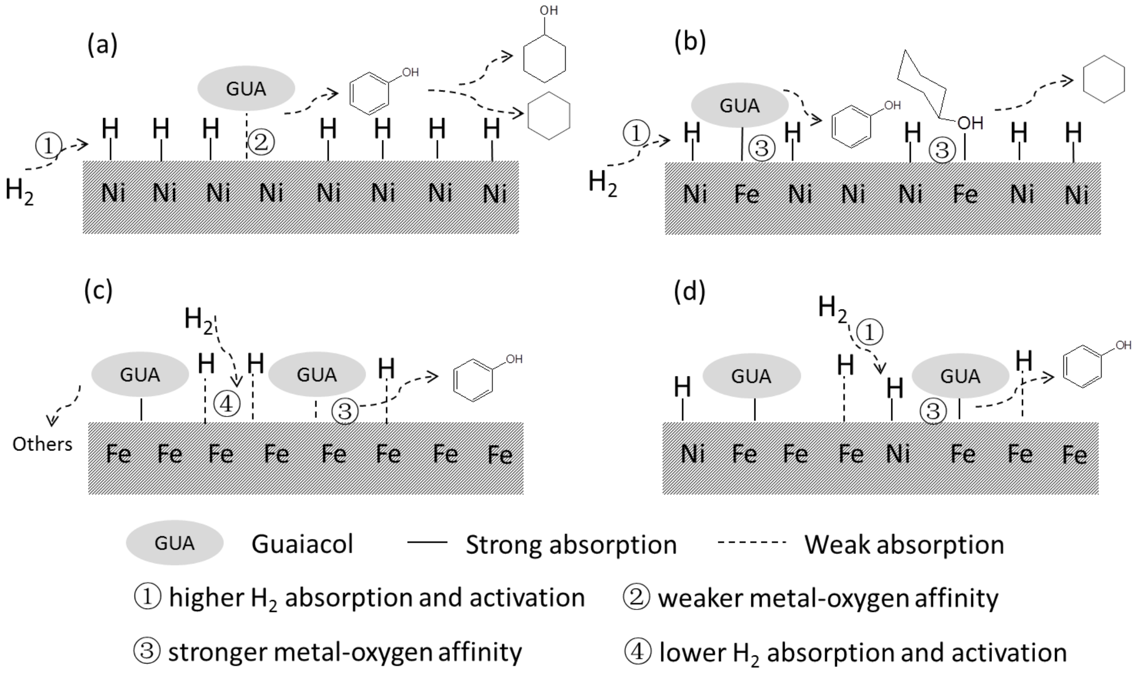

**Scheme 2** Plausible reaction mechanisms for HDO of guaiacol over different catalysts: (a) Ni/CNT, (b) Ni$_5$–Fe$_1$/CNT, (c) Fe/CNT, and (d) Ni$_1$–Fe$_5$/CNT.

**Table 1** Physicochemical properties of Ni–Fe/CNT catalysts with different Ni/Fe atomic ratios

| Sample | Total M loading[a] / wt. % | Ni/Fe atomic ratio | | $S_{BET}$ / $m^2\ g^{-1}$ | $D_{pore}$ / nm | CO uptake / μmol $g^{-1}$ | Average particle size /nm | | R[c] value |
|---|---|---|---|---|---|---|---|---|---|
| | | By ICP | By XPS | | | | by XRD[b] | by TEM | |
| CNT–O | – | – | – | 147 | 24.1 | – | – | – | 0.89 |
| Ni/CNT | 7.07 | ∞ | ∞ | 145 | 15.3 | 72.4 | 9.2 | 8.7 | 0.84 |
| $Ni_5$–$Fe_1$/CNT | 6.59 | 4.41:1 | 1.69:1 | 145 | 14.8 | 67.5 | 7.7 | 7.3 | 0.85 |
| $Ni_2$–$Fe_1$/CNT | 6.02 | 2.08:1 | 0.59:1 | 149 | 15.8 | 37.6 | 7.0 | 6.9 | 0.85 |
| $Ni_1$–$Fe_1$/CNT | 5.93 | 1.06:1 | – | 153 | 15.2 | 21.3 | 6.3 | 6.2 | 0.87 |
| $Ni_1$–$Fe_2$/CNT | 6.38 | 0.46:1 | – | 159 | 13.4 | 14.3 | 5.9 | 5.7 | 0.89 |
| $Ni_1$–$Fe_5$/CNT | 5.49 | 0.27:1 | – | 150 | 17.5 | 13.7 | 5.3 | 5.3 | 0.89 |
| Fe/CNT | 6.42 | 0 | 0 | 138 | 23.0 | 11.6 | 6.0 | 5.1 | 0.90 |

[a] Metal loading was determined by ICP-OES.

[b] The average particle size was calculated by the Scherrer equation using 2θ at 44.28°.

[c] R value represents the $I_D/I_G$ intensity ratio in Raman spectra.

**Table 2** Catalytic performance of Ni/CNT, Fe/CNT and bimetallic Ni–Fe catalysts with different reduction temperatures[a]

| Catalyst | Entry | RT[b] / K | Particle size / nm | Conv. / % | C6-ring selec. / % | | | | | C1 product selec. / % | | TOF[c] / $h^{-1}$ |
|---|---|---|---|---|---|---|---|---|---|---|---|---|
| | | | | | 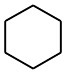 | 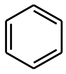 | 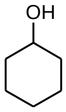 | 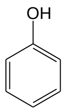 | Others | $CH_4$ | MeOH | |
| Ni/CNT | 1 | 673 | 9.2 | 79.0 | 53.0 | 0.3 | 31.7 | 4.4 | 10.6 | 82.2 | 9.3 | 275.9 |
| | 2 | 773 | 13.5 | 80.2 | 24.7 | 0.7 | 58.3 | 1.0 | 15.3 | 58.9 | 30.4 | 262.3 |
| | 3 | 873 | 16.0 | 77.0 | 4.6 | 1.1 | 69.7 | 10.4 | 14.2 | 33.0 | 50.9 | 258.9 |
| $Ni_5$–$Fe_1$ /CNT | 4 | 673 | 7.7 | 96.8 | 83.4 | 3.2 | 12.7 | 0.0 | 0.7 | 85.4 | 14.6 | 370.2 |
| | 5 | 773 | 8.3 | 96.7 | 67.5 | 6.0 | 23.0 | 0.0 | 3.5 | 76.0 | 22.0 | 350.6 |
| | 6 | 873 | 11.2 | 99.0 | 55.8 | 4.2 | 31.9 | 0.0 | 8.1 | 61.7 | 38.3 | 342.5 |
| $Ni_1$–$Fe_5$ /CNT | 7 | 673 | 5.3 | 47.2 | 2.5 | 0.9 | 10.4 | 83.3 | 2.9 | 67.6 | 24.5 | 104.5 |
| | 8 | 773 | 5.7 | 41.3 | 2.4 | 0.8 | 13.2 | 79.4 | 4.2 | 40.7 | 14.9 | 98.7 |
| | 9 | 873 | 5.2 | 41.5 | 2.5 | 0.6 | 12.5 | 81.0 | 3.4 | 38.9 | 13.8 | 96.4 |
| Fe/CNT | 10 | 673 | 6.0 | 17.2 | 0.4 | 0.5 | 0.7 | 40.4 | 58.0 | 64.9 | 24.3 | 41.1 |
| | 11 | 773 | 6.0 | 19.3 | 0.0 | 0.0 | 1.6 | 92.9 | 5.5 | 57.5 | 19.6 | 45.8 |
| | 12 | 873 | 11.5 | 8.4 | 1.5 | 0.8 | 2.6 | 90.8 | 4.4 | 44.5 | 5.6 | 30.4 |

[a] Reaction conditions: $WLHSV_{GUA} = 6.0\ h^{-1}$, $P(H_2) = 3.0$ MPa, $H_2$/GUA molar ratio = 50, $T = 573$ K.

[b] RT represents the reduction temperature of the catalyst.

[c] TOF value is based on the metal dispersions by particle size estimated by TEM and XRD.